Reverse Microemulsion Synthesis, Structure, and Luminescence of Nanosized $REPO_4:Ln^{3+}$ (RE = La, Y, Gd, or Yb, and Ln = Eu, Tm, or Er)

Paulo C. de Sousa Filho and Osvaldo A. Serra*

Departamento de Química, Faculdade de Filosofia, Ciências e Letras de Ribeirão Preto, Universidade de São Paulo, Ribeirão Preto, SP, Brazil

Received: October 18, 2010; Revised Manuscript Received: November 22, 2010

A surfactant-mediated solution route for the obtainment of nanosized rare-earth orthophosphates of different compositions ($LaPO_4:Eu^{3+}$, $(Y,Gd)PO_4:Eu^{3+}$, $LaPO_4:Tm^{3+}$, $YPO_4:Tm^{3+}$, and $YbPO_4:Er^{3+}$) is presented, and the implications of the morphology control on the solids properties are discussed. The solids are prepared in water-in-heptane microemulsions, using cetyltrimethylammonium bromide and 1-butanol as the surfactant and cosurfactant; the alteration of the starting microemulsion composition allows the obtainment of ~30 nm thick nanorods with variable length. The morphology and the structure of the solids were evaluated through scanning electron microscopy and through powder X-ray diffractometry; dynamic light scattering and thermal analyses were also performed. The obtained materials were also characterized through vibrational (FTIR) and luminescence spectroscopy (emission/excitation, luminescence lifetimes, chromaticity, and quantum efficiency), where the red, blue, and upconversion emissions of the prepared phosphors were evaluated.

1. Introduction

The use of rare-earth (RE)-based phosphors began around the 1970s, aiming at the generation of the three primary colors in cathode ray tubes and fluorescent lamps. Since then, the evolution and diversification of RE-bearing inorganic phosphors have followed the development of new visualization/lighting technologies, in the sense that they must be compatible in terms of stability and efficiency with the excitation source and the working method of each particular system.[1−5] The great interest in trivalent lanthanoid cations arises from their unique intraconfigurational f−f transitions, which can occur as sharp and intense emission lines. For example, the Eu^{3+} red and the Tb^{3+} green emissions are extensively employed in many luminescent devices, besides finding many analytical applications.[3] In addition, due to its chemical stability and high emission color purity, and although it normally has very low emission intensities, Tm^{3+} remains a very promising candidate for generation of the blue color in such systems, to substitute for the unstable Eu^{2+} ions that are currently used.[3,4,6]

Within the wide range of applications of RE-containing phosphors, the rare-earth orthophosphates ($REPO_4$) have a prominent role in most of these technological fields, because of their physicochemical inertia (stability under high temperatures, high-energy excitations, and chemical decomposition).[7−9] For example, these compounds are very suitable phosphors for vacuum ultraviolet (VUV; $\lambda_{exc} < 200$ nm) applications, such as plasma display panels and Hg-free fluorescent lamps. In these cases, their applicability arises from their excitability in the VUV range, high visible light reflectivity, and resistance under operational conditions and against annealings for deposition.[4−9] Moreover, besides conventional linear processes, $REPO_4$ phosphors can also efficiently present near-infrared (NIR) upconversion luminescence, thus being applicable as NIR detectors, lasers, and imaging agents.[10−12] In particular, the expected low toxicity and the photochemical stability of luminescent or upconverting RE-bearing phosphates allow their use as biolabels in noninvasive medical diagnostic procedures after a proper biofunctionalization process.[13−15] In most of these examples, the morphology of the solids is a limiting factor for their usefulness, and high surface-to-volume ratios are required for good efficiencies to be achieved. Under VUV excitation, for instance, the low penetrability of this radiation implies that most of the luminescence phenomena occur on the surface atoms, so that nanosized solids are preferred.[4,5] On the other hand, particle size distribution must be narrow and with a mean value that is compatible with the expected biological role in the case of biolabeling applications, so that an efficient targeting is attained.[15]

In summary, all of these applications are limited by a delicate balance among morphological, compositional (purity, activator/sensitizer concentrations, and stability), and structural-spectroscopic (appropriate site symmetry for activator ions) properties. Thus, to attain control of these properties at the molecular level, efficient synthetic procedures that are clean and inexpensive and that consume low energy are required. Because routes involving reactions in solution are preferred to fulfill these requirements, much attention is currently being paid to wet-chemical methods for the production of nanosized $REPO_4$, such as colloidal syntheses[16] and solvothermal[17−19] and hydrothermal[20−22] precipitations. In this sense, surfactant-mediated processes,[9,11,23,24] mainly those based on reverse microelumsions, are also being widely explored since they allow a bottom-up control of the molecular organization of the nanostructure design, the so-called "zeptoliter chemistry".

Therefore, this work deals with the establishment of a synthetic route for the preparation of $REPO_4$ in water-in-oil microemulsions, with the evaluation of the effect of the starting composition of the microemulsions on the morphology of the materials. It has been possible to demonstrate that $REPO_4$ of controllable morphology and with several compositions can be obtained via a simple procedure carried out in solution, showing that highly stable phosphors with different luminescent behavior can be prepared for a wide range of applications.

* To whom correspondence should be addressed. Phone: +55-16-3602-3746or +55-16-3602-4376. E-mail: osaserra@usp.br.

10.1021/jp109988a
Published on Web 12/15/2010

2. Experimental Section

2.1. Synthesis. Rare-earth nitrate stock solutions (1.0 mol L^{-1}) were prepared through the dissolution of the previously calcined rare-earth oxides (La_2O_3, Eu_2O_3, Er_2O_3, Tm_2O_3, Yb_2O_3, 99.99%, Rhône-Poulenc/Rhodia; Gd_2O_3, 99.99%, Strem-Chemicals; Y_2O_3, 99.99%, Alfa-Aesar) in concentrated nitric acid. The pH of these solutions was adjusted to ~4 through evaporation of the acid in excess. In the synthetic procedures, the $RE(NO_3)_3$ solutions were properly mixed so that the following compositions would be attained (1.0 mol L^{-1} in RE^{3+}): $La_{0.99}Eu_{0.01}$, $Y_{0.64}Gd_{0.35}Eu_{0.01}$, $La_{0.99}Tm_{0.01}$, $Y_{0.99}$,$Tm_{0.01}$, and $Yb_{0.95}Er_{0.05}$. For further evaluation of the effect of a complexing agent on the morphology of the solids, $(La_{0.99}Eu_{0.01})(NO_3)_3$ solutions containing 1.0 mol L^{-1} citric acid (H_3cit) were also prepared and used in the syntheses. The procedure employed for the preparation of the nanosized powders was the same in all cases, and the orthophosphate source was always $NaH_2PO_4 \cdot H_2O$ (99+%, Aldrich). First, the two starting water-in-oil microemulsions were prepared. The utilized organic phase was *n*-heptane (99.5%, J.T. Baker), and the water:oil volume ratio was kept at 1:10 in all the preparations. Cetyltrimethylammonium bromide (CTAB; 98%, Vetec, previously recrystallized twice from ethanol) and 1-butanol (99.5%, Merck) were used as the surfactant and cosurfactant, respectively (at a fixed CTAB:1-butanol mass ratio of 70%). The microemulsions, which were limpid and monophasic in all cases, were prepared by dispersing the appropriate volumes of rare-earth nitrate or NaH_2PO_4 (0.55 mol L^{-1}) aqueous solutions in *n*-heptane (so that a 10% PO_4^{3-} excess would be obtained). Different water:CTAB (ω_0) molar ratios (ω_0 = 15, 30, 40, or 50) were employed. The microemulsions were aged for 24 h before any measurement and before being used. The reactions were initiated by adding the $RE(NO_3)_3$-containing microemulsion dropwise to the microemulsion-containing NaH_2PO_4 under vigorous stirring, and the system was then kept under reflux for 24 h to attain high yields and high particle homogeneity. It is worth mentioning that both microemulsions must have the same ω_0 ratio. Finally, the products were separated from the resulting monophasic microemulsions by centrifugation. The solids were washed with water until the washing tested negative for bromide ions (as detected with saturated $AgNO_3$), which was followed by washing with an additional 50 mL of water and then 25 mL of ethanol. The solids were dried in vacuum in a desiccator over silica (yield 70−85%). In all cases, hydrated solids were obtained. For elimination of the hydration waters, the solids were treated with triethyl orthoformate (TEOF; Aldrich, 99%) in anhydrous EtOH (~100 mg of solid/10 mL of EtOH/5 mL of TEOF) for 4 h under reflux. After separation by centrifugation and washing with anhydrous EtOH, the solids were annealed at 400 °C for 24 h in air. For further comparison and mainly for the luminescence measurements, the solids were also postannealed at 900 °C for 2 h, thus resulting in hexagonal-to-monoclinic or hexagonal-to-tetragonal structural conversions in the phosphates.

2.2. Characterization. Morphological analysis of the obtained powders was accomplished with a Jeol JSM 7401F field emission microscope (SEM−FEG) and a Zeiss EVO50 scanning electron microscope coupled to an IXRF Systems 500 digital processing accessory (SEM−energy-dispersive system, EDS). The structural analysis was performed by powder X-ray diffractometry (XRD) in a Siemens D5005 diffractometer, using the Cu Kα radiation (1.541 Å) and a graphite monochromator. The thermal behavior of the solids was evaluated in a TA Instruments SDT simultaneous differential thermal analysis−thermogravimetric analysis (DTA−TGA) Thermal Analyst 2100, operating under a synthetic air atmosphere (100 mL min^{-1} flux) at a heating rate of 10 °C min^{-1}. The vibrational spectroscopy data of the materials were obtained by Fourier transform infrared (FTIR) spectroscopy using KBr pellets in an ABB Bomen FTLA2000-100 spectrometer with 2 cm^{-1} resolution.

The hydrodynamic data of the microemulsions and solids were acquired by dynamic light scattering at 298 K in a Malvern Instruments Zetasizer 3000 HSA photon-correlation spectrometer. For particle size determination in the microemulsions (Supporting Information), the viscosity and the refractive index of pure *n*-heptane were employed; for the ζ-potential determination, ~10^{-4} mol L^{-1} suspensions of the solids were prepared using different solutions as dispersing media (0.01 mol L^{-1} acetic acid/acetate buffer for pH 2 and 4, 0.01 mol L^{-1} ammonium acetate for pH 7, and 0.01 mol L^{-1} ammonia/ammonium buffer for pH 10 and 12). The luminescence spectra and lifetime measurements (with direct excitation on the solids) were recorded on a Horiba-Jobin Yvon SPEX Triax 550 FluoroLog 3 spectrofluorometer equipped with a continuous 450 W xenon arc lamp and a pulsed 150 W xenon lamp as sources, besides a Hamamatsu R928P photomultiplier and a Peltier-cooled SPEX Synapse charge-coupled device (CCD) as detectors. The emission and excitation spectra were corrected with relation to the detector sensitivity and lamp intensity in the monitored wavelength range by using the apparatus software.

3. Results and Discussion

3.1. Morphological and Structural Characterization. Figures 1−3 display the SEM−FEG micrographs of the $LaPO_4$:Eu^{3+} powders obtained at different ω_0 ratios (15, 30, 40, 50). The results clearly show that the proposed method is adequate for morphological control of the $REPO_4$ synthesis at the nanoscale. As seen in Figure 1, the prepared powders are composed by microaggregates of elongated nanostructures of variable length, which are dependent on the starting ω_0 ratio. Nevertheless, in all cases, a high thickness uniformity of 20−30 nm is observed, regardless of the water:surfactant ratio.

At higher surfactant concentrations (ω_0 = 15−30, Figure 1a,b), quite similar nanorods of 50−100 nm length are obtained. They occur as micrometric aggregates of ~1 μm length and 250−500 nm thickness. In situations of lower surfactant content (ω_0 = 40, Figure 1c), a distinct microemulsion molecular organization may lead to the formation of 30 nm thick nanowires of expressive lengths (>1 μm). This reflects a possible lamellar organization in this microemulsion system, in which the water pools may be confined with a higher degree of continuity, which would give rise to quite elongated $REPO_4$ nanostructures. On the other hand, the solids obtained at ω_0 = 50 (Figure 1d) present a lower degree of particle agglomeration, being composed by well-defined nanorods of 100−200 nm length.

The observed elongated structures suggest that the rate of inorganic nucleation is higher than the rate of micellar fusion/dissociation, so that an approximately cylindrical particle is expected for each micellar collision. Therefore, further micellar dynamic exchange may favor faster subsequent growth at the ends of the initial particle, which should yield the elongated structures that later aggregate and segregate from the microemulsion (Figure S1, Supporting Information).[25] The fact that the particle thickness is independent of the ω_0 ratio indicates that the nucleation and the formation of the nanorod seeds are very similar in all cases; further differentiation (affected by the microemulsion composition) takes place in the subsequent processes of particle growth.

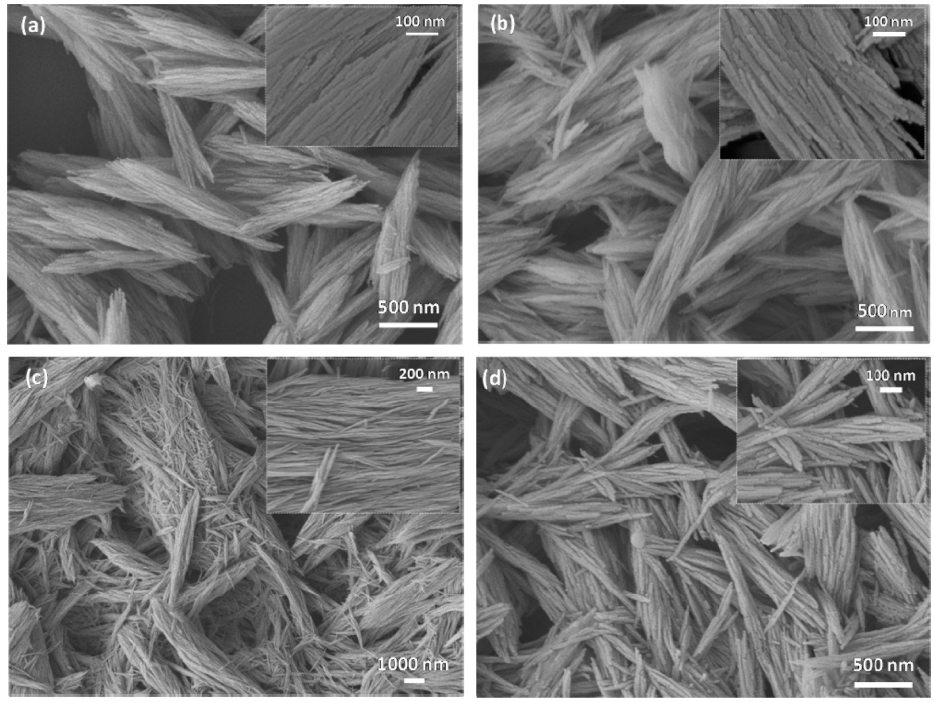

Figure 1. SEM−FEG micrographs of $LaPO_4:Eu^{3+}$ obtained in the absence of H_3cit at different water:surfactant starting ratios: (a) $\omega_0 = 15$, (b) $\omega_0 = 30$, (c) $\omega_0 = 40$, (d) $\omega_0 = 50$.

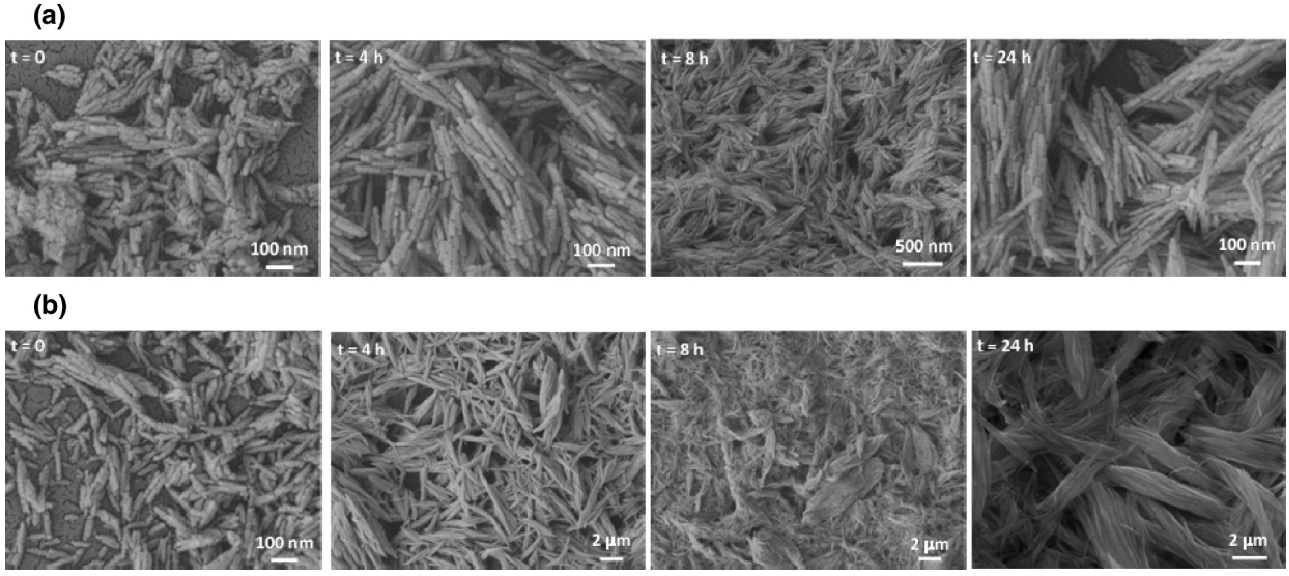

Figure 2. Evaluation of the reaction time effect on the $LaPO_4:Eu^{3+}$ particle size and morphology in a synthesis carried out with (a) $\omega_0 = 50$ and (b) $\omega_0 = 40$ in the absence of H_3cit.

To evaluate the evolution of particle morphology along the reaction, aliquots of ~1 mL of the reaction mixtures were collected at different times. The SEM−FEG images of the solids [obtained at time 0 (completion of the mixture of the starting microemulsions) and 4, 8, and 24 h of reaction for mixtures with $\omega_0 = 40$ and $\omega_0 = 50$] after separation by centrifugation are shown in Figure 2. The micrographs illustrate the lack of influence of the ω_0 ratio on particle nucleation and formation of nanorod seeds since, at $t = 0$, practically identical particles are observed in the two monitored cases. Moreover, the occurrence of particle growth at the ends of the nanorod seeds is also evidenced by the micrographs.

On the basis of the observed behavior, the addition of a chelating agent to the aqueous precursors should diminish the rate of inorganic nucleation, thus retarding the growth at the ends of the nanoparticles. Figure 3 depicts the SEM−FEG micrographs of the solids obtained using $RE(NO_3)_3$ solutions containing 1.0 mol L^{-1} H_3cit. The images show that, as expected, the complexing action of the citric acid species in solution enables nanorod stabilization by avoiding subsequent growth. Moreover, the particles present a lower degree of aggregation after the synthesis, which is also an effect of the action of H_3cit. Again, the thickness of the particles remains practically the same, while the length of the nanorods can be controlled by the starting ω_0 ratio ($\omega_0 = 15$, 30−50 nm; $\omega_0 = 30$, 70−90 nm; $\omega_0 = 40$, 100−150 nm; $\omega_0 = 50$, 70−90 nm).

The stability of the different hydrated $LaPO_4:Eu^{3+}$ nanoparticles in suspension was electrokinectically assessed by determination of the ζ-potential, which allows for estimation of the electrostatic repulsion of the particles. To this end, suspensions

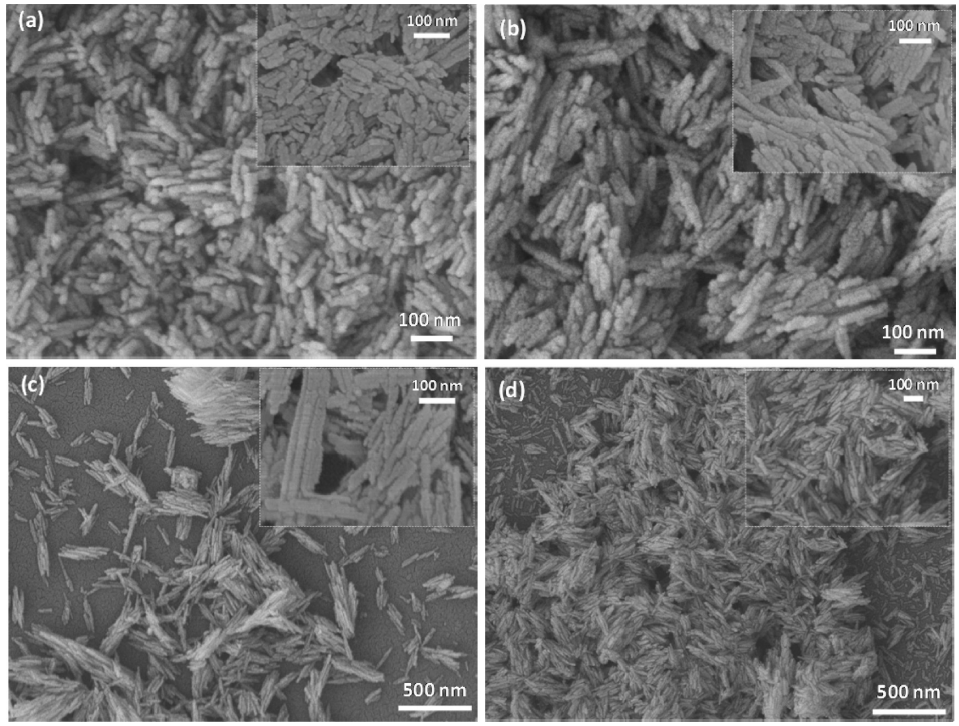

Figure 3. SEM−FEG micrographs of $LaPO_4:Eu^{3+}$ obtained with the addition of H_3cit to the $RE(NO_3)_3$-containing microemulsions: (a) $\omega_0 = 15$, (b) $\omega_0 = 30$, (c) $\omega_0 = 40$, (d) $\omega_0 = 50$.

of the prepared powders were submitted to electrophoretic mobility measurements by dynamic light scattering. Figure 4a demonstrates that the particles obtained in the absence of H_3cit present the same behavior with regard to pH, showing moderate colloidal stability under extreme acid or basic conditions ($30 < |\zeta| < 50$ mV). Moreover, a slight change in the isoelectric point (i.e., pH at which $\zeta = 0$) is observed for the different ω_0 ratios (pH_{iep} follows the order $\omega_0 = 15 < \omega_0 = 30 < \omega_0 = 40 \approx \omega_0 = 50$), which can be related to the morphological differences and, thus, to the area available for the surface charges. The same behavior is observed for the pH_{iep} values of the solids obtained in the presence of H_3cit, but the mean isoelectric point value is lower in the latter cases. The profile of the plot of ζ-potential against pH is also different for the latter solids, with two maxima at pH 4 and 10. This can be attributed to the presence of a small amount of residual citric acid species on the surface of the particles, which affects the overall surface charge because of their acid−base equilibria.

The thermal behavior of the synthesized powders was also evaluated by TGA−DTA analysis, which showed that the solids present almost the same behavior (independent of the starting ω_0 ratio). As seen from the thermal analysis curves (Supporting Information), the decomposition of the nanopowders occurs in two endothermic steps. The first one appears in the temperature range between 50 and 150 °C and is associated with the loss of physisorbed water and surface hydration waters. The second decomposition step, centered at 200 °C, corresponds to the loss of "zeolitic" water molecules (i.e., those occupying defined crystallographic sites at the channels present in the rhabdophane structure),[26] as well as the beginning of conversion from the hexagonal to monoclinic phase. The DTA curves reveal that the loss of water molecules is followed by the endothermic structural conversion, which is completed between 600 and 800 °C. As shown in Tables S2 and S3 (Supporting Information), the composition of the solids can be estimated by considering these two steps of water loss. The results indicate that all solids display the same degree of structural hydration (zeolitic waters)

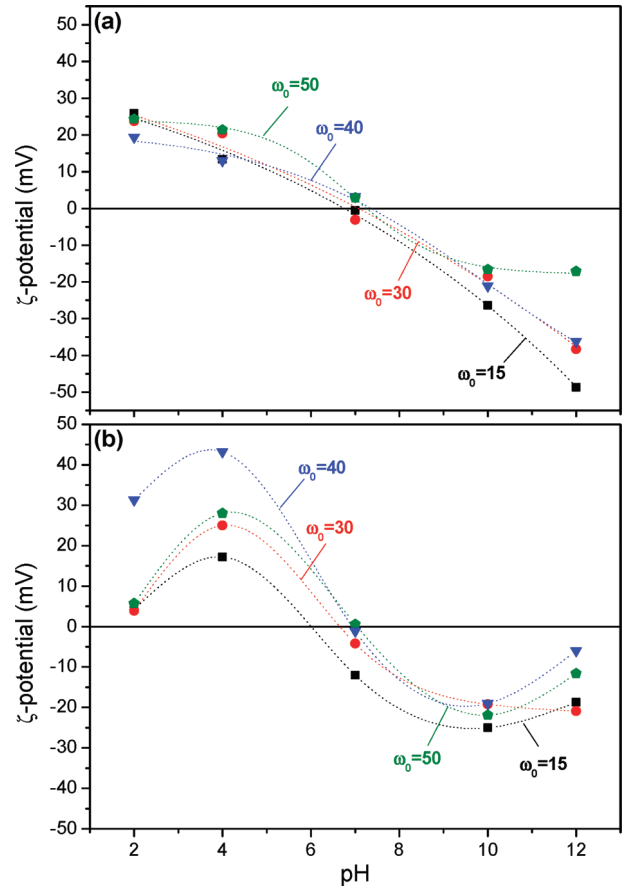

Figure 4. ζ-potential as a function of pH for the hydrated $LaPO_4:Eu^{3+}$ nanoparticles synthesized (a) in the absence of H_3cit and (b) with addition of H_3cit.

since they present the same percentage mass loss in the second step, which in turn results in the $(La,Eu)PO_4 \cdot 0.6H_2O$ approximate composition. The overall composition, obtained by

also taking the surface waters into account, is virtually the same for the $\omega_0 = 15$, 30, and 50 (obtained in the absence of H_3cit) preparations [(La,Eu)$PO_4 \cdot 1.4H_2O$], which is in agreement with their similar morphological properties. On the other hand, the solid obtained at $\omega_0 = 40$ exhibits a higher degree of physisorbed water, namely, a (La,Eu)$PO_4 \cdot 3.3H_2O$ overall composition, associated with the occurrence of nanowires instead of nanorods. The solids synthesized from H_3cit-containing microemulsions display a very similar behavior, with the same two decomposition steps, besides an additional exothermic step centered at ~300 °C, which is related to the oxidation of the adsorbed H_3cit. In the latter case, the compositional calculations yield a similar value of structural hydration (around 0.6), besides a similar overall water content (of about 1.1−1.3), compared to those of the previous samples.

The powder X-ray diffractograms attest that the proposed microemulsion synthesis leads to the production of hydrated phosphates. In the case of the $LaPO_4:Ln^{3+}$ samples, the solids present the rhabdophane-type ($REPO_4 \cdot xH_2O$; RE = La, Ce, Nd; $0.5 < x < 1$) primitive hexagonal structure, whose spatial groups are $P6_222$ (D_6^4, No. 180) and $P3_121$ (D_3^4, No. 152).[26] Figure 5a corresponds to the XRD patterns of the hydrated $LaPO_4:Eu^{3+}$ samples. In all the cases, the occurrence of largely broadened peaks indicates that the solids are composed by nanostructures. Nevertheless, because the particles are not spherical, the application of the usual Debye−Scherrer method (with $K = 0.9$) for estimation of the crystallite size was not performed due to lack of a proper shape parameter. Moreover, no peaks of other phases or impurities were detected, thus attesting to the purity of the solids. The observed diffraction profiles slightly differ from the rhabdophane pattern with regard to the relative intensities of some peaks, which indicates the occurrence of anisotropic growth during the formation of the crystallites. In this case, for example, crystal growth in the [010] plane ($2\theta \approx 14.5°$) is defavored with regard to that in the [011] ($2\theta \approx 20°$) and [100] ($2\theta \approx 25°$) planes. This is related to the structure-directing action of the reverse-micelle aggregates, which, as already discussed, favor the growth processes at the ends of the nanoparticle seeds in the micellar collisions, thus resulting in elongated structures. Figure 5b illustrates that the TEOF treatment for elimination of hydration waters is mild, so it does not significantly affect the structures of the solids since the hexagonal rhabdophane phase is still dominant. Nevertheless, some additional peaks, which are related to the presence of the monazite phase, are observed, giving evidence that a small amount of the hexagonal phase is collapsed, thereby yielding the monoclinic phase. As shown in Figure 5c, the solids assume the monoclinic monazite structure (of $P2_1/m$ (C_{2h}^2) space group, No. 11) after the calcinations at 900 °C, again without peaks of phases due to contaminants. The diffractograms also present considerable peak broadening, indicating that the solids maintain a nanostructural character even after the calcinations. Moreover, the crystallite anisotropic growth is also evidenced by the large intensification of the [012] reflection (at $2\theta \approx 30.9°$) compared with the [−120] ($2\theta \approx 28.9°$) and [200] ($2\theta \approx 26.8°$) reflections. The $LaPO_4:Eu^{3+}$ solids synthesized in the presence of H_3cit present very similar diffraction behavior (Supporting Information), with the same anisotropic growths before and after the calcinations, besides large peak broadening.

The powder X-ray diffractograms of the other synthesized phosphates are presented in the Supporting Information (Figures S9−S13). As expected, the $LaPO_4:Tm^{3+}$ phosphor has properties very similar to those of the Eu^{3+}-doped lanthanum phosphates. The samples containing yttrium or ytterbium as the main host components [(Y,Gd)$PO_4:Eu^{3+}$, $YPO_4:Tm^{3+}$, and $YbPO_4:Er^{3+}$] are also obtained in their hydrated forms, with a rhabdophane-type $P6_222/P3_121$ structure, thus being isostructural to the hexagonal $YPO_4 \cdot 0.8H_2O$ (JCPDS 420082). In these cases, no contaminations of the more stable body-centered tetragonal xenotime-type phase (of $I4_1/amd$ (D_{4h}^{19}), No. 141, space group) are observed in the hydrated or TEOF-treated solids, thus attesting to the high selectivity of the microemulsion synthesis with respect to the obtainment of hexagonal phosphates. After the calcinations, these phosphates assume the tetragonal xenotime structure. The calcined $YPO_4:Tm^{3+}$ and $YbPO_4:Er^{3+}$ samples present diffraction patterns which are coherent with

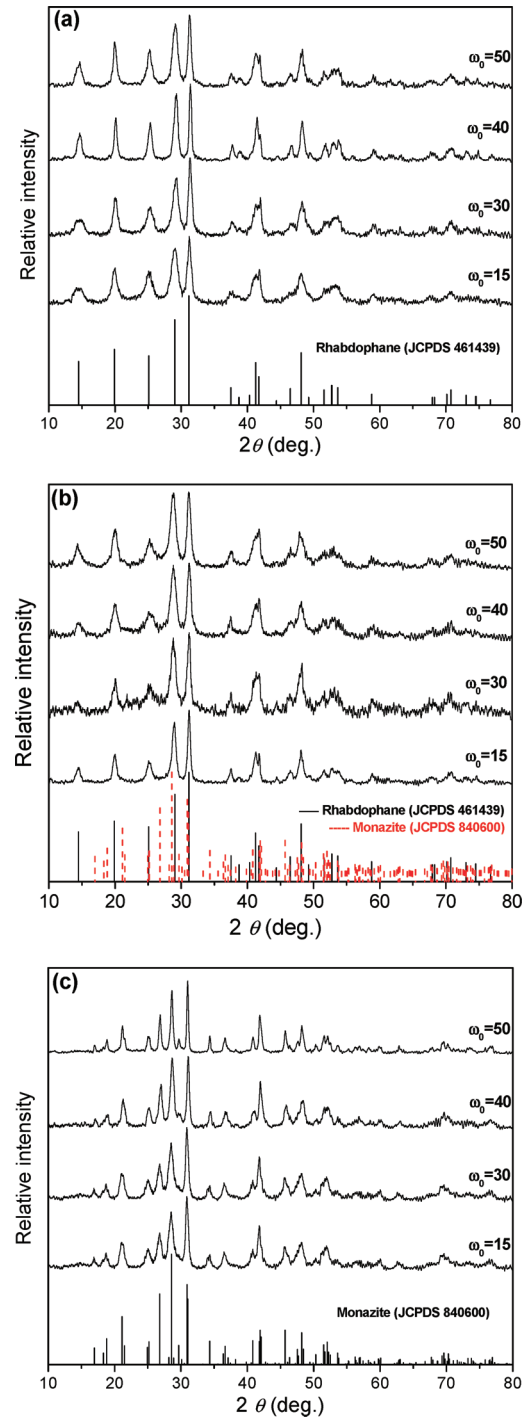

Figure 5. Powder X-ray diffractograms of the $LaPO_4:Eu^{3+}$ samples synthesized in the absence of H_3cit: (a) hydrated, (b) TEOF-treated, (c) calcined.

the xenotime standard. On the other hand, because of the high concentration of Gd^{3+} ions (which tend to form a monoclinic $GdPO_4$ phase), the relative intensity of some reflections is strongly changed in the case of the (Y,Gd)PO_4:Eu^{3+} sample. This indicates the occurrence of very prominent preferential growths, which is in agreement with what has been observed for similar preparations.[8] Nevertheless, good incorporation of the Gd^{3+} ions into the YPO_4 host is confirmed by the absence of reflection peaks that are not related to the tetragonal phase.

3.2. Vibrational Spectroscopy. The infrared spectra of the prepared phosphates (Supporting Information) evidence the purity of the obtained compounds since bands related to hydrogen phosphates, which can lead to contaminations with polyphosphates after the thermal treatment, at ~900 cm^{-1} (P−OH stretching) are absent. Moreover, the efficiency of the washing processes is confirmed by the absence of bands ascribed to the surfactant molecules, such as C−H stretching (at ~2900 cm^{-1}) and CH_2 scissoring (at ~1450 cm^{-1}) vibrations. In the $LaPO_4$:Eu^{3+} samples prepared in the presence of H_3cit, additional bands of low intensity at 2925 and 2853 cm^{-1} and at 1412 cm^{-1} are observed, which are related to the presence of small amounts of citrate species on the particle surface.[22] In the hydrated $LaPO_4$:Ln^{3+} samples, a characteristic profile of orthophosphate groups under C_2 symmetry is observed, which is in agreement with the space group of the solids in the hexagonal structure.[26,27] In these cases, three groups of absorption bands are observed, one of low intensity related to the P−O symmetric stretching (ν_1, A) at 950 cm^{-1}, one broad and intense band composed by at least three components related to P−O antisymmetric stretching (ν_3, A + 2B) centered at 1050 cm^{-1}, and three bands ascribed to the O−P−O antisymmetric deformation (ν_4, A + 2B) at 613, 570, and 542 cm^{-1}. As yttrium phosphate-based samples were also obtained as rhabdophane-type hydrated solids, in these samples the orthophosphate ions also occupy C_2 sites, giving rise to a band unfolding similar to the previously described ones. As already mentioned, for the hexagonal $LaPO_4$ phosphors, the TEOF treatment leads to partial conversion of the hexagonal phase into the monoclinic one. This is evidenced by the appearance of an additional component in the ν_4 bands, besides the intensification of the ν_1 stretching band. The same occurs for the hexagonal yttrium phosphate-based samples. After the thermal treatment at 900 °C, the hexagonal $LaPO_4$:Ln^{3+} samples are completely converted into monoclinic phosphates. In these cases, the PO_4^{3-} groups occupy C_s or C_1 sites; under such symmetries, all the combinations of fundamental vibrations are IR-allowed, leading to high band unfoldings. In these samples, the P−O symmetric stretching band (ν_1) occurs at 952 cm^{-1}, the P−O antisymmetric stretching band (ν_3) presents five observable components at 1120 (shoulder), 1090, 1060, 1015, and 990 cm^{-1}, and the antisymmetric bending (ν_4) appears as a doublet pair with frequencies at 613, 578, 565, and 542 cm^{-1}. On the other hand, the YPO_4:Ln^{3+} and $YbPO_4$:Er^{3+} samples are converted into tetragonal phosphates after the calcinations; in these cases, the PO_4^{3-} groups occur as distorted tetrahedra with D_{2d} symmetry. In such cases, the orthophosphate ions have only two IR-active vibrations, one ascribed to the ν_3 stretching (B_2 + E) at ~1100 and ~1025 cm^{-1} and another ascribed to the ν_4 deformation (B_2 + E) at ~635 and ~530 cm^{-1}. In the calcined (Y,Gd)PO_4:Eu^{3+} sample, the presence of additional bands in the ν_4 region denotes the coexistence of another phosphate phase, which can be ascribed, as further discussed, to a small amount of monoclinic $GdPO_4$ phase.

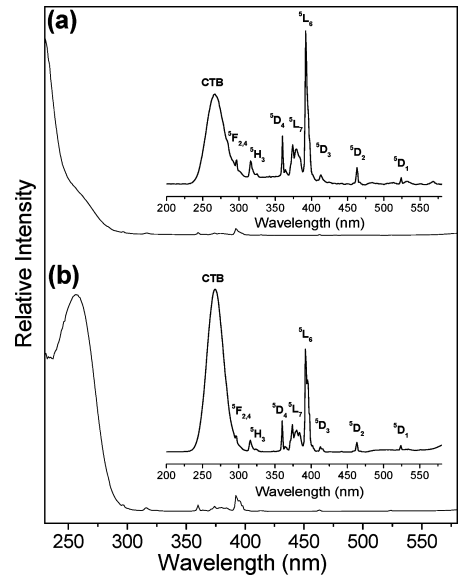

Figure 6. Excitation spectra (λ_{em} = 616 nm) of the $LaPO_4$:Eu^{3+} samples (a) after the TEOF treatment and (b) after calcination at 900 °C (in this case, obtained at $\omega_0 = 50$). Insets: excitation spectra without the lamp intensity correction.

3.3. Luminescence Spectroscopy. ***3.3.1. Eu^{3+}-Doped Phosphates.*** The emission and excitation spectra of the $LaPO_4$:Eu^{3+} samples obtained at different conditions are shown in Figures 6−9. The as-prepared (hydrated) solids present very low luminescence as a consequence of the presence of a large number of quenching species (OH groups).[3,4] On the other hand, after the TEOF treatment and drying, the solids start to display more significant emissions. The excitation spectra of the TEOF-treated $LaPO_4$:Eu^{3+} samples (Figure 6a) are, for all ω_0 ratios and regardless of the presence of H_3cit, composed by a broad band which appears as a shoulder at 265 nm, assigned to the $O^{2-} \rightarrow Eu^{3+}$ charge transfer band (CTB), besides the characteristic f−f Eu^{3+} absorptions, the $^5L_6 \leftarrow {}^7F_0$ transition at 394 nm being the most intense line. There is no expressive shift in the CTB position with regard to the different ω_0 ratios, which means that the solid band structure was not significantly affected by the morphological alterations. In these cases, the emission spectra of the solids (Figure 7a) under CTB or $^5L_6$ excitation are composed by a set of broad $^5D_0 \rightarrow {}^7F_J$ bands with a large unfolding, which indicates the occupation of low-symmetry sites.[3,4,28] This is due to the coexistence of the hexagonal and monoclinic phases in the TEOF-treated phosphates, besides the low degree of crystallinity of the samples, which together result in the occupation of multiple sites with similar properties. This is also clearly indicated by the existence of two bands attributed to the $^5D_0 \rightarrow {}^7F_0$ transition at 577.0 and 577.5 nm. Besides, the occurrence of broadened bands leads to chromaticity coordinates[29] (Table 1) which are relatively far from the ones required for a red phosphor.[4]

In the excitation spectra of the calcined solids (Figure 6b), a strong intensification of the CTB at 265 nm compared with the f−f absorptions is observed as a consequence of the higher crystallinity of these samples. Once more, the solids obtained with different ω_0 ratios and in the presence or absence of H_3cit possess essentially the same emission/excitation profile. Besides, no alterations in the position or in the relative intensities of the f−f absorptions are noticed, thus revealing large site similarity before and after the calcinations. Moreover, the occupation of sites with high centrosymmetric character is also evidenced by the low intensity of the $^5D_2 \leftarrow {}^7F_0$ transition at 464 nm, which

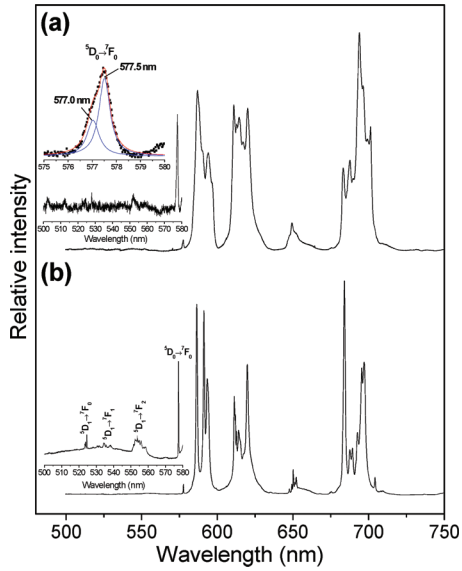

Figure 7. Emission spectra ($\lambda_{exc} = 394$ nm) of the $LaPO_4$:Eu^{3+} samples (a) after the TEOF treatment and (b) after calcination at 900 °C (in this case, obtained at $\omega_0 = 50$).

takes place through forced electric dipole and vibronic coupling mechanisms and is also hypersensitive to the site symmetry with regard to an inversion center ($\Delta J = 2$).[3,28] The emission spectra of the solids (Figure 7b) are composed by the $^5D_0 \leftarrow {}^7F_J$ lines with the maximum $2J + 1$ unfolding for a single site, which attests to the occupation of a low-symmetry site (C_1, C_s, C_i) and is in agreement with the sites available in the $P2_1/m$ monoclinic structure. In this case, the $^5D_0 \rightarrow {}^7F_0$ transition occurs as a sharp line ($\sim$10 cm^{-1} width) at 17316 cm^{-1}, thereby indicating that the postannealing results in the monoclinic phase only, with a single symmetry site for the Eu^{3+} ions. Despite the predominance of the orange $^5D_0 \rightarrow {}^7F_1$ emissions over the $^5D_0 \rightarrow {}^7F_2$ ones, the sharpening of the emission bands after the calcinations and the high intensity of the $^5D_0 \rightarrow {}^7F_4$ transition (in the deep red region) lead to very high emission red color purities ($x \approx 0.67$, $y \approx 0.33$, Table 1) which are exactly the red NTSC standards.[4]

The luminescence lifetimes of the synthesized solids were also investigated and are listed in Table 1. The decay curves are presented in the Supporting Information. The TEOF-treated samples display a biexponential behavior as a result of the coexistence of the hexagonal and monoclinic phases, thus giving rise to at least two emitting centers. The deconvolution of the experimental decay curves yielded lifetimes of $\tau_1 \approx 3.9$ and $\tau_1 \approx 0.8$ ms, approximately, for all the cases, regardless of the composition of the starting microemulsion. In spite of being relatively high (in agreement with the elimination of the hydration waters), these luminescence lifetimes are quite low compared with those observed after the calcinations (Table 1), which clearly display a monoexponential excited-state decay with lifetimes around 5.0 ms. This is indeed expected, because the low crystallinity of the samples in the first cases provides many nonradiative means of excited-state deactivation. Nevertheless, the lifetimes observed for the calcined $LaPO_4$:Eu^{3+} samples are quite high, which is probably related to both the high crystallinity of the samples and their nanostructural character. The high crystallinity guarantees a high atomic organization, which provides efficient activator separation (to diminish the rate of concentration quenching) and a very low interaction of the emitting states with the lattice phonons. On the other hand, the nanostructural character leads to higher surface areas and, consequently, to larger amounts of surface defects, which can act as traps for the luminescent centers by interacting with the emitting states and increasing their luminescence lifetimes.[30]

Figure 8 shows that the (Y,Gd)PO_4:Eu^{3+} excitation spectra display, besides the characteristic Eu^{3+} lines, very intense lines ascribed to Gd^{3+} absorptions (mainly the $^6I_J \leftarrow {}^8S_{7/2}$ and $^6P_J \leftarrow {}^8S_{7/2}$ transitions at 271 and 303−310 nm) which dominate the spectra. This evidences an efficient sensitizing action of the Gd^{3+} ions in this compound, thus enabling the exploration of "photon-cascade" or "downconversion" processes (quantum yields greater than unity) with this red phosphor under proper excitation at $\sim$200 nm.[4] In this sample, the f−f lanthanoid absorptions are also accompanied by an intense charge transfer band centered at 230 nm. The occurrence of a CTB at higher energies compared with those observed in the $LaPO_4$:Eu^{3+} samples are related to the stronger ionic character of the YPO_4 host, which leads to a low-lying valence band (VB). Consequently, the separation between the VB and the divalent state of the europium ions (f^7) is increased, leading to a CTB at higher energies.[31]

In the emission spectrum of the TEOF-treated (Y,Gd)PO_4:Eu^{3+} sample (Figure 9a), a large predominance of the $^5D_0 \rightarrow {}^7F_1$ transition over the $^5D_0 \rightarrow {}^7F_2$ transition indicates the possible occupation of sites with a high centrosymmetric character, which is in agreement with the occupation of D_2 sites in the hexagonal structure. This high intensity of orange emissions does not compromise the purity of the red color emission of this preparation ($x \approx 0.67$ and $y \approx 0.33$). In this solid, the coexistence of at least two cation sites is evidenced by the occurrence of a very broad ($\sim$90 cm^{-1} width) $^5D_0 \rightarrow {}^7F_0$ transition, which can be deconvoluted into at least two components (Figure 9a, inset). This is a consequence of the coexistence of D_2 and D_{2d} sites of the hexagonal and tetragonal structures, as a result of a partial conversion due to the TEOF treatment. Moreover, the Gd^{3+} ions can give rise to another monoclinic phase since the pure gadolinium phosphate can occur with the monazite structure.[27] Even though the amount of these secondary phases is so low that it cannot be detected by XRD, their occurrence is easily noticed via Eu^{3+} spectroscopy due to the high sensitivity of this technique. The excited-state kinetic behavior of this sample can be well fitted by a biexponential decay curve, which corroborates with the occurrence of two Eu^{3+} emitting centers in the (Y,Gd)PO_4 host. The deconvolution of the experimental decay curves yields lifetimes of $\tau_1 \approx 3.84$ and $\tau_2 \approx 0.62$ ms.

The emission spectrum of the calcined (Y,Gd)PO_4:Eu^{3+} sample displays a strong intensification of the $^5D_0 \rightarrow {}^7F_2$ transition with regard to $^5D_0 \rightarrow {}^7F_1$, which is a consequence of the occupation of the D_{2d} sites in the tetragonal structure. This fact, in addition to the narrowing of the emission bands and the high intensity of the $^5D_0 \rightarrow {}^7F_4$ transition, leads to very high chromaticities for this compound ($x \approx 0.68$, $y \approx 0.34$). As for the TEOF-treated sample, the emission profile does not depend on the excitation wavelength (on the CTB at 230 nm, on the Gd^{3+} ^6I_J level at 271 nm, or on the Eu^{3+} $^5L_6$ level at 394 nm). In the case of the calcined powder, the occurrence of more than one symmetry site for the Eu^{3+} ion is also evidenced by the presence of two components centered at 579.6 and 580.0 nm, ascribed to the $^5D_0 \rightarrow {}^7F_0$ transition. The occurrence of two Eu^{3+} sites can be associated, as already discussed, with a small amount of monoclinic $GdPO_4$ coexisting with the tetragonal (Y,Gd)PO_4 phase. Nevertheless, despite the presence of two Eu^{3+} centers, the excited-state decay curves of this sample can

TABLE 1: Luminescence Lifetimes, Radiative and Nonradiative Decay Rates, Quantum Efficiencies, and Chromaticity Coordinates[29] Obtained for the Eu^{3+}-Doped Phosphates under 394 nm Excitation[a]

	lifetime (ms)					chromaticity	
	τ_1	τ_2	A_{RAD} (s^{-1})	A_{NRAD} (s^{-1})	η (%)	x	y
$LaPO_4:Eu^{3+}$ (TEOF-treated)							
$\omega_0 = 15$	3.90	0.79	233	142	62	0.637	0.360
$\omega_0 = 30$	3.85	0.75	231	143	62	0.636	0.362
$\omega_0 = 40$	3.87	0.90	234	144	62	0.639	0.358
$\omega_0 = 50$	3.68	0.70	226	145	61	0.638	0.359
$LaPO_4:Eu^{3+}$ (calcined)							
$\omega_0 = 15$	4.76		199	10	95	0.664	0.334
$\omega_0 = 30$	5.04		192	6	97	0.670	0.328
$\omega_0 = 40$	4.53		203	18	92	0.667	0.332
$\omega_0 = 50$	5.56		178	2	99	0.672	0.327
$(Y,Gd)PO_4:Eu^{3+}$ (TEOF-treated)	3.84	0.62	151	280	35	0.668	0.331
$(Y,Gd)PO_4:Eu^{3+}$ (calcined)	3.72		224	99	69	0.676	0.323

[a] Luminescence lifetimes are accurate within 5%; the calculated parameters are accurate within 10%.

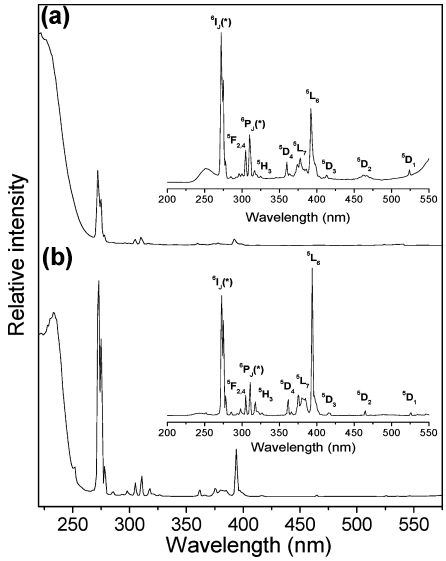

Figure 8. Excitation spectra (λ_{em} = 590 nm) of the prepared $(Y,Gd)PO_4:Eu^{3+}$ nanopowder (a) after the TEOF treatment and (b) after calcination at 900 °C (the asterisks indicate Gd^{3+} excitation lines).

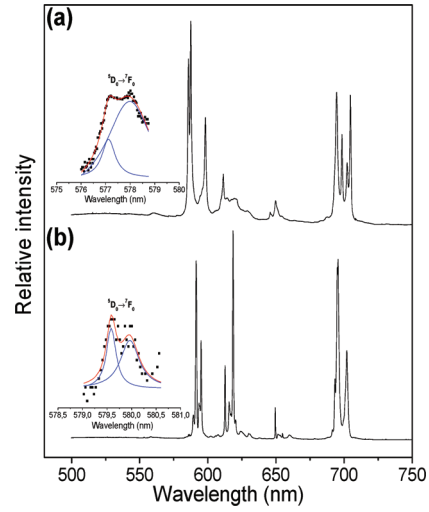

Figure 9. Emission spectra (λ_{exc} = 271 nm) of the (a) hexagonal (after the TEOF treatment) and (b) tetragonal (after calcination at 900 °C) $(Y,Gd)PO_4:Eu^{3+}$ sample. Insets: amplification of the $^5D_0 \rightarrow {}^7F_0$ transition ranges.

always be well fitted by monoexponential functions, regardless of the monitored wavelengths (λ_{em} = 589.0 ± 0.5, 591.0 ± 0.5, 595 ± 10, or 612 ± 10 nm) or the excitation mechanism (^6I_J or $^5L_6$) (Supporting Information). This characterizes pseudo-first-order excited-state kinetics, which can be the result of an efficient energy transfer mechanism from one site to another (thus reducing the lifetime of one of the emitting centers considerably) or of the fact that the two centers have quite similar luminescence lifetimes. The second explanation seems to be more appropriate since monitoring of the individual components of the $^5D_0 \rightarrow {}^7F_1$ transition with 0.5 nm resolution yields similar lifetimes (Supporting Information).

For better evaluation of the Eu^{3+} luminescent behavior in the synthesized phosphate hosts, the radiative (A_{RAD}) and nonradiative (A_{NRAD}) decay rates, as well the excited-state quantum efficiencies, were calculated from the emission spectra and luminescence lifetimes.[32,33] The emission quantum efficiency of a determined excited state is defined as the ratio between the rate of radiative deactivation and the total rate of deactivation. Considering the Einstein spontaneous emission coefficients (A_{RAD}), the emission quantum efficiency is given by

$$\eta = \frac{A_{RAD}}{A_{RAD} + A_{NRAD}} \tag{1}$$

The total rate of excited-state deactivation ($A_{RAD} + A_{NRAD}$) is equal to the reciprocal of the mean excited-state lifetime:

$$A_{RAD} + A_{NRAD} = \tau^{-1} \tag{2}$$

Therefore, the quantum efficiency can be written as

$$\eta = A_{RAD}\tau \tag{3}$$

Taking the emission of the Eu^{3+} $^5D_0$ level, the radiative rate of excited-state deactivation can be considered as a sum of the particular rates for each of the $^5D_0 \rightarrow {}^7F_J$ ($J = 0-6$) transitions:

$$A_{RAD} = \sum_J A_{0-J} \tag{4}$$

For being allowed through a magnetic dipole mechanism, the $^5D_0 \rightarrow {}^7F_1$ transition has a calculable rate of radiative deactiva-

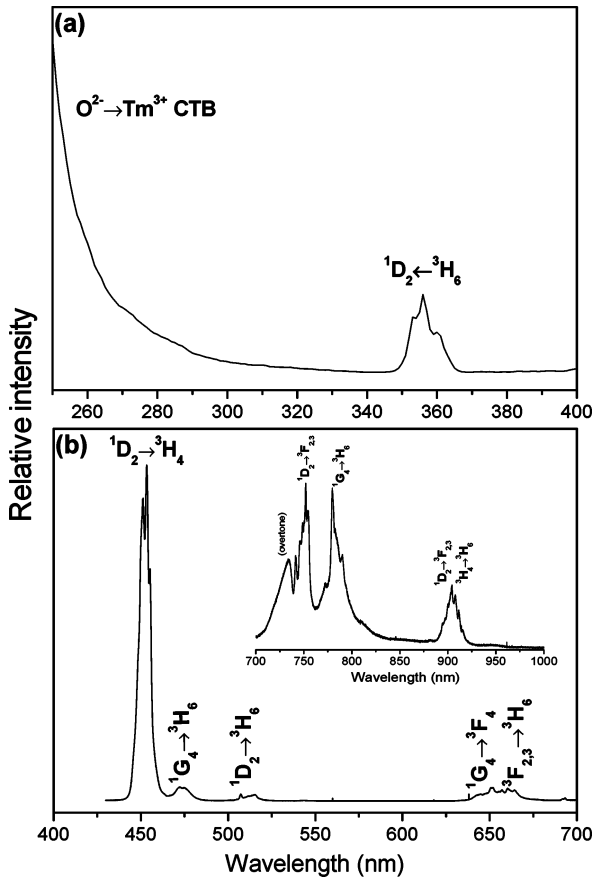

Figure 10. (a) Excitation (λ_{em} = 450 nm) and (b) emission (λ_{exc} = 358 nm) of the $LaPO_4$:Tm^{3+} sample (calcined at 900 °C).

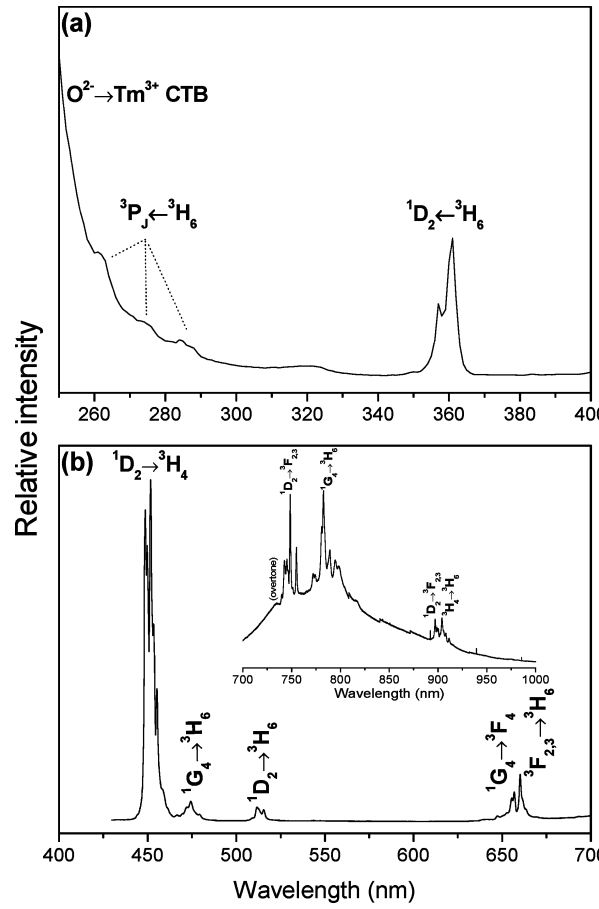

Figure 11. (a) Excitation (λ_{em} = 450 nm) and (b) emission (λ_{exc} = 360 nm) of the YPO_4:Tm^{3+} sample (calcined at 900 °C).

tion and can be used as a reference for the determination of the other A_{0-J} rates. The value of A_{0-1} can be calculated from

$$A_{0-1} = 0.31 \times 10^{-11} n^3 \sigma_{0-1}{}^3 \quad (5)$$

where n is the refractive index of the material and σ_{0-1} is the energy baricenter of the $^7F_1$ level (calculated from the emission spectra). The refractive index considered for our calculations is 1.75 since the tabulated values found for the monazite and xenotime vary between 1.70 and 1.80. The other A_{0-J} radiative rates are calculated from

$$A_{0-J} = A_{0-1}\frac{S_{0-J}\sigma_{0-1}}{S_{0-1}\sigma_{0-J}} \quad (6)$$

where σ_{0-J} is the energy baricenter of the ^7F_J level and S_{0-J} is the area corresponding to the $^5D_0 \rightarrow {}^7F_J$ transition in the emission spectrum. Therefore, by applying eqs 3 and 4, the emission quantum efficiencies are calculated from the emission spectra. In the cases where two distinct Eu^{3+} emitting centers exist, a mean lifetime obtained by fitting the experimental curves for monoexponential decays was utilized. The TEOF-treated $LaPO_4$:Eu^{3+} samples display relatively high quantum yields, around 60%, thus attesting that, despite the relatively low temperature used during the drying procedure, efficient red phosphors are obtained. In these cases, the most prominent contribution for the nonradiative decay rate arises from the low crystallinity of the samples, which provides multiphonon pathways for excited-state deactivation. In the (Y,Gd)PO_4:Eu^{3+} phosphor, this effect is more pronounced due to the probable coexistence of many phosphate phases, thus resulting in a higher A_{NRAD} rate. After the calcination, this effect is largely reduced, resulting in a ~70% quantum efficiency. Nevertheless, the more interesting result is observed for the calcined $LaPO_4$:Eu^{3+} phosphors, which, for having a very long lifetime, possess quantum yields close to unity, as a result of nonradiative decay rates close to zero. In this way, the synthetic approach allows one to obtain very efficient Eu^{3+}-doped phosphors whose high crystallinity and nanostructural character provide a means for a very long lived luminescence with a quite high quantum efficiency.

3.3.2. Blue-Emitting Phosphors. The proposed route was applied for the synthesis of tetragonal and monoclinic blue-emitting Tm^{3+}-doped phosphates. The excitation spectra of $LaPO_4$:Tm^{3+} and YPO_4:Tm^{3+} (Figures 10a and 11a) are, in both cases, composed by a broad band at energies higher than 33 500 cm^{-1} (as a result of the $O^{2-} \rightarrow Tm^{3+}$ charge transfer) and by the main Tm^{3+} f−f absorption at ~360 nm, ascribed to the $^1D_2 \leftarrow {}^3H_6$ transition. In the YPO_4:Tm^{3+} sample, this transition occurs as a sharper band due to the lower unfolding of the $^{2S+1}L_J$ levels in the D_{2d} sites of the tetragonal structure; besides, in this case the absorptions to the higher Tm^{3+} levels ($^3P_J \leftarrow {}^3H_6$) can also be detected. The emission spectra of the Tm^{3+}-doped phosphates under $^1D_2$ excitation (Figures 10b and 11b) are dominated by the blue $^1D_2 \rightarrow {}^3H_4$ emission at 450 nm, and their luminescence is visible to the eye (despite its low brightness), appearing as blue. This results in high blue color purities for these compounds (x = 0.17 and y = 0.07 for $LaPO_4$:Tm^{3+} and x = 0.20 and y = 0.09 for YPO_4:Tm^{3+}), which are acceptable for applications as blue phosphors according to the NTSC standards (x = 0.14, y = 0.08).[4] The other transitions within

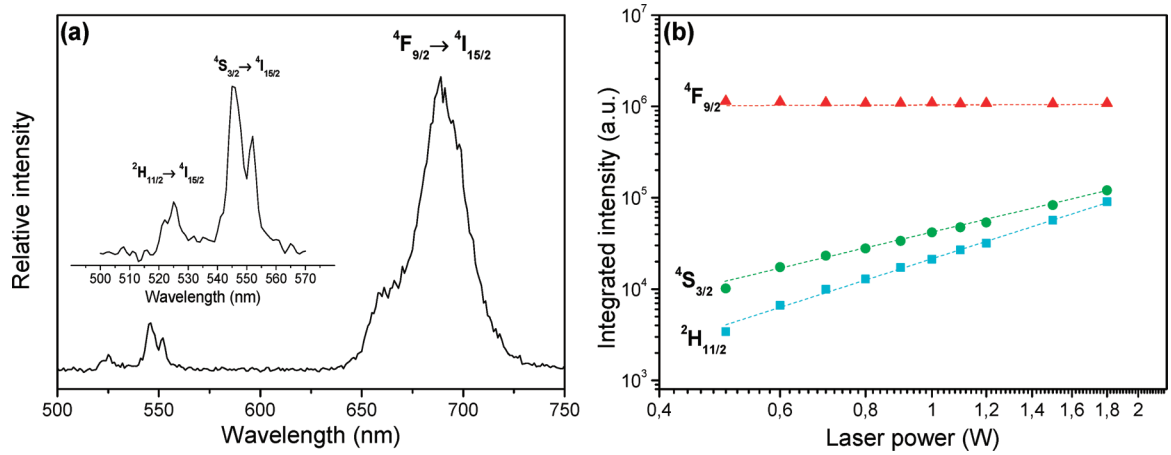

Figure 12. (a) Upconversion luminescence spectrum of $YbPO_4:Er^{3+}$ under 980 nm laser excitation (500 mW). (b) Laser power dependence of the upconversion intensity measured at the $^2H_{11/2} \rightarrow {}^4I_{15/2}$ (λ = 525 mn), $^4S_{3/2} \rightarrow {}^4I_{15/2}$ (λ = 545 mn), and $^4F_{9/2} \rightarrow {}^4I_{15/2}$ (λ = 650 nm) transitions.

the Tm^{3+} f^{12} configuration result in low-intensity emissions in the visible and NIR ranges, and the integration of the $LaPO_4$:Tm^{3+} emissions results in an almost monochromatic color, as seen in the chromaticity diagram (Figure S24, Supporting Information). Although it presents narrower bands, the YPO_4:Tm^{3+} sample has the lower color purity due to the slightly larger intensity of the other visible emissions arising from the $^1D_2$, $^1G_4$, and $^3F_{2,4}$ levels. Nevertheless, although they present a low luminescence yield due to the competitive infrared emissions within the complicated Tm^{3+} energy levels, the high chemical stability and high emission color purity of these materials make them suitable for applications under VUV excitation.

3.3.3. Upconversion Luminescence of $YbPO_4:Er^{3+}$. Figure 12a shows the upconversion (UC) luminescence spectrum of the $YbPO_4:Er^{3+}$ sample under 980 nm laser excitation. A measurable luminescence appears only after the thermal treatment at 900 °C since a higher crystallinity is achieved only in this way, thus avoiding the nonradiative deactivation of the intermediary $^4I_{11/2}$ and the emitting $^2H_{11/2}$, $^4S_{3/2}$, and $^4F_{9/2}$ levels in the Yb^{3+}/Er^{3+} couple. Although the pure tetragonal $YbPO_4$ is known to display a cooperative UC luminescence,[3] the UC efficiency of the Yb^{3+}/Er^3 couple in this host is expected to be very low, because the higher phonon energy in this material takes place at ~1100 cm^{-1}. This leads to very strong vibronic interactions of the involved ions with their surroundings, thus diminishing the lifetime of the intermediary levels and reducing the global efficiency of the phosphor. Nevertheless, in this case, this is overcome by the high concentration of the sensitizer Yb^{3+} ions, which leads to a strong absorption at 980 nm as a result of the spin-allowed $^2F_{5/2} \leftarrow {}^2F_{7/2}$ transition, followed by the $Yb^{3+} \rightarrow Er^{3+}$ energy transfer, which in turn gives rise to the $^4I_{11/2}$ excited state of Er^{3+}. Another NIR photon is then transferred from the Yb^{3+} ions, thereby leading to the population of the $Er^{3+4}F_{7/2}$ level and resulting in its green ($^2H_{11/2}$, $^4S_{3/2} \rightarrow {}^4I_{15/2}$) and red ($^4F_{9/2} \rightarrow {}^4I_{15/2}$) emissions. In this case, the spectrum is dominated by the spin-allowed $^4F_{9/2} \rightarrow {}^4I_{15/2}$ Er^{3+} transition, thus resulting in a predominantly red UC luminescence.

The variation of the UC luminescence intensity (computed as the integrated area of the monitored transition) as a function of the laser power (Figure 12b) results, as expected, in a linear behavior in the log(intensity) against log(power) plot, with slopes of 2.4 and 1.8 for the $^2H_{11/2} \rightarrow {}^4I_{15/2}$ and $^4S_{3/2} \rightarrow {}^4I_{15/2}$ transitions, respectively. Within the experimental error, these values corroborate with a two-photon excitation scheme for the UC process in this phosphate. On the other hand, due to its high intensity, the $^4F_{9/2} \rightarrow {}^4I_{15/2}$ transition displays an independence of the laser power, indicating that an NIR photon excitation saturation occurs even at 500 mW. This is a result of a very efficient nonradiative decay from the populated $^4F_{7/2}$ level to the emitting $^4F_{9/2}$ level (probably due to interactions with lattice phonons and defects), which makes $^4F_{9/2} \rightarrow {}^4I_{15/2}$ the most prominent transition in the UC process, so that its power dependency can only be measured at lower laser powers.

4. Conclusion

In summary, a versatile solution route has been evaluated for the preparation of a wide range of nanosized rare-earth orthophosphates. The synthetic approach, based on the nanoreactor concept, involves the dispersion of the reactive precursors in the water pools of reverse microemulsions (using CTAB/1-butanol as the surfactant mixture and *n*-heptane as the continuous phase). The procedures lead to the production of elongated nanoparticles or nanowires of uniform thickness, whose length and degree of aggregation can be controlled by varying the water:surfactant ratio or by the addition of a complexing agent for the RE^{3+} ions (e.g., citric acid). This growth process is related to the microemulsion dynamics, in which the rate of precipitation is higher than the rate of micellar dissociation, thus favoring the elongation of the particle seeds. As expected, the complexing action of H_3cit retards the inorganic precipitation, thus stabilizing the formed nanorods and diminishing their degree of aggregation.

The procedure favors the formation of hydrated hexagonal phosphates for both the lighter and heavier lanthanoids, with visible effects of the structure-directing action of the microemulsion systems on the powder XRD patterns. The analyses carried out herein confirm the purity of the synthesized materials, whose degree of hydration is also dependent on the observed morphology. Despite the low temperatures employed here, the TEOF treatment has been shown to efficiently eliminate hydration waters, resulting in Eu^{3+}-doped phosphors with a relatively high quantum yield. Nevertheless, after the calcinations at 900 °C, these phosphates present even higher luminescence intensities and quantum efficiencies close to unity. Moreover, the synthesized $LaPO_4:Tm^{3+}$ and $YPO_4:Tm^{3+}$ samples efficiently display blue emissions with high color purity, and the $YbPO_4:Er^{3+}$ phosphor presents intense red upconversion under NIR excitation. In conclusion, the proposed synthetic method is very suitable for the production of several nanosized RE-containing luminescent phosphates, whose composition and morphology can be designed for a wide range of applications.

Acknowledgment. We thank the Brazilian agencies CAPES, CNPq (Proc. 480003/2009-2, O.A.S.), FAPESP (Proc. 2008/09266-5, P.C.d.S.F.), RENAMI, and inct-INAMI for financial support. We are also grateful to Professors E. Tfouni, M. E. D. Zaniquelli, S. J. L. Ribeiro, and J. M. A. Caiut for utilization of the instrumental facilities and to Drs. C. M. C. P. Manso and R. F. Silva for helpful discussions.

Supporting Information Available: Thermal analysis curves, FTIR spectra of the obtained powders, microemulsion dynamic light scattering and nanoparticle ζ-potential determination data, additional X-ray diffractograms, additional EDS spectra and SEM-EDS mapping images, chromaticity diagrams, additional luminescence spectra, and decay curves for luminescence lifetime determination. This material is available free of charge via the Internet at http://pubs.acs.org.

References and Notes

(1) Feldman, C.; Jüstel, T.; Ronda, C.; Schmidt, P. *Adv. Funct. Mater.* **2003**, *13*, 511–516.

(2) Jüstel, T.; Nikol, H.; Ronda, C. *Angew. Chem., Int. Ed.* **1998**, *37*, 3085–3103.

(3) Blasse, G.; Grabmaier, B. C. *Luminescent Materials*; Springer-Verlag: Berlin, 1994.

(4) Yen, W. M., Shinoya, S., Yamamoto, H., Eds. *Phosphor Handbook*, 2nd ed.; CRC Press: Boca Raton, FL, 2007.

(5) Moine, B.; Bizarri, G. *Opt. Mater.* **2006**, *28*, 58–63.

(6) Rao, R. P. *J. Lumin.* **2005**, *113*, 271–278.

(7) Niinistö, L.; Leskelä, M. In *Handbook on the Physics and Chemistry of Rare Earths*; Gschneidner, K. A., Jr., Eyring, L., Eds.; Elsevier: Amsterdam, 1987; Chapter 59.

(8) de Sousa Filho, P. C.; Serra, O. A. *J. Fluoresc.* **2008**, *18*, 329–337.

(9) de Sousa Filho, P. C.; Serra, O. A. *J. Lumin.* **2009**, *129*, 1664–1668.

(10) Heer, S.; Lehmann, O.; Haase, M.; Güdel, H.-U. *Angew. Chem., Int. Ed.* **2003**, *42*, 3179–3182.

(11) Ghosh, P.; Oliva, J.; de la Rosa, E.; Haldar, K. K.; Solis, D.; Patra, A. *J. Phys. Chem. C* **2008**, *112*, 9650–9658.

(12) Jungowska-Hornowska, W.; Macalik, L.; Lisiecki, R.; Godlewska, P.; Matraszek, A.; Szczygiel, I.; Hanuza, J. *Mater. Chem. Phys.* **2009**, *117*, 262–267.

(13) Meiser, F.; Cortez, C.; Caruso, F. *Angew. Chem., Int. Ed.* **2004**, *43*, 5954–5957.

(14) Ashokan, A.; Menon, D.; Nair, S.; Koyakutty, M. *Biomaterials* **2010**, *31*, 2606–2616.

(15) Wang, F.; Tan, W. B.; Zhang, Y.; Fan, X.; Wang, M. *Nanotechnology* **2006**, *17*, R1–R13.

(16) Buissette, V.; Moreau, M.; Gacoin, T.; Boilot, J.-P.; Chane-Ching, J.-Y.; Le Mercier, T. *Chem. Mater.* **2004**, *16*, 3767–3773.

(17) Riwotzki, K.; Meyssamy, H.; Kornowski, A.; Haase, M. *J. Phys. Chem. B* **2000**, *104*, 2824–2828.

(18) Willinger, M.-G.; Clavel, G.; Di, W.; Pinna, N. *J. Ind. Eng. Chem.* **2009**, *15*, 883–887.

(19) Yang, P.; Quan, Z.; Li, C.; Hou, Z.; Wang, W.; Lin, J. *J. Solid State Chem.* **2009**, *182*, 1045–1054.

(20) Yang, M.; You, H.; Jia, G.; Huang, Y.; Song, Y.; Zheng, Y.; Liu, K.; Zhang, L. *J. Cryst. Growth* **2009**, *311*, 4753–5758.

(21) Lin, S.; Dong, X.; Jia, R.; Yuan, Y. *J. Mater. Sci: Mater. Electron.* **2010**, *21*, 38–44.

(22) Li, C.; Hou, Z.; Zhang, C.; Yang, P.; Li, G.; Xu, Z.; Fan, Y.; Lin, J. *Chem. Mater.* **2009**, *21*, 4598–4607.

(23) Xing, Y.; Li, M.; Davis, S. A.; Mann, S. *J. Phys. Chem. B* **2006**, *110*, 1111–1113.

(24) Bu, W.-B.; Hua, Z.-L.; Zhang, L.-X.; Chen, H.-R.; Huang, W.-M.; Shi, J.-L. *J. Mater. Res.* **2004**, *19*, 2807–2811.

(25) Hopwood, J. D.; Mann, S. *Chem. Mater.* **1997**, *9* (8), 1819–1828.

(26) Mooney, R. L. C. *Acta Crystallogr.* **1950**, *3*, 337–340.

(27) Kijkowska, R.; Cholewka, E.; Duszak, B. *J. Mater. Sci.* **2003**, *38*, 223–228.

(28) Bünzli, J.-C. G. In *Lanthanide Probes in Life, Chemical and Earth Sciences*; Bünzli, J.-C. G., Choppin, G. R., Eds.; Elsevier: Amsterdam, 1989; Chapter 7.

(29) Santa-Cruz, P. A.; Teles, F. S. *Spectra Lux Software*, version 2.0; Ponto Quântico Nanodispositivos/RENAMI: Recife, Brazil, 2003.

(30) Aitasalo, T.; Dereń, P.; Hölsä, H.; Jungner, H.; Krupa, J.-C.; Lastusaari, M.; Legendziewicz, J.; Niittykoski, J.; Strek, W. *J. Solid State Chem.* **2003**, *171*, 114–122.

(31) Li, L.; Zhang, S. *J. Phys Chem. B* **2006**, *110*, 21438–21443.

(32) de Sá, G. F.; Malta, O. L.; de Mello Donegá, C.; Simas, A. M.; Longo, R. L.; Santa-Cruz, P. A.; Silva, E. F., Jr. *Coord. Chem. Rev.* **2000**, *196*, 165–195.

(33) Kodaira, C. A.; Brito, H. F.; Malta, O. L.; Serra, O. A. *J. Lumin.* **2001**, *101*, 11–21.

JP109988A